Barite Growth Rates as a Function of Crystallographic Orientation, Temperature, And Solution Saturation State

Mélanie Vital, Damien Daval, Gilles Morvan, Daniel E Martinez, Michael J Heap

Barite growth rates as a function of crystallographic orientation, temperature, and solution saturation state

Mélanie Vital[1,2,*], Damien Daval[2,*], Gilles Morvan[2], Daniel E. Martinez[1], Michael J. Heap[3]

[1]Instituto de Geología de Costas y Cuaternario (UNMDP-CIC) – Instituto de Investigaciones Marinas y Costeras (CONICET-UNMDP). Mar del Plata, Argentina.

[2]Université de Strasbourg, CNRS / ENGEES – EOST, Laboratoire d'Hydrologie et de Géochimie de Strasbourg, 1 Rue Blessig, 67084 Strasbourg, France.

[3]Géophysique Expérimentale, Institut de Physique de Globe de Strasbourg (UMR 7516 CNRS, Université de Strasbourg/EOST), 5 rue René Descartes, 67084 Strasbourg cedex, France.

[*]corresponding authors:

M. Vital (ingagr.melanie.vital@gmail.com ; Tel.: 005492235288191)

D. Daval (ddaval@unistra.fr ; Tel.: 003 68 85 05 56)

Abstract

Barite growth kinetics was investigated as a function of crystallographic orientation for temperatures between 10 and 70 °C, and initial saturation indices (*SI*) of 1.1 and 2.1. The growth rates were estimated for (001), (210), and (101) faces using vertical scanning interferometry. Overall, face-specific barite growth rates ($r^{(hkl)}$) can be successfully described by the following rate law:

$$r^{(hkl)} = A^{(hkl)}.\exp\left(-E_a^{(hkl)}/RT\right).(10^{SI}-1)$$

where $A^{(hkl)}$and $E_a^{(hkl)}$ represent the face-specific Arrhenius pre-exponential factor and activation energy, respectively, R is the gas constant, and T refers to the absolute temperature. In addition, because of the modest growth anisotropy of the various investigated faces, the following isotropic rate law can be used to satisfactorily account for the measured rate data:

$$r^{(hkl)} = A.\exp(-E_a/RT).(10^{SI}-1)$$

with average values of A = exp(13.59) nm.h^{-1} and E_a = 35.0 ± 2.5 kJ.mol^{-1}. Over the range of conditions investigated in the present study, our results suggest that barite growth kinetics is surface-controlled, while possibly verifying the principle of detailed balancing and micro-reversibility. These results imply that previous modeling exercises of steady-state barite growth based on isotropic rate laws may remain valid, at least over the range of conditions investigated in the present study.

***Keywords**:* barite; anisotropic growth; geothermal reservoir; scaling; growth rate law

1. Introduction

Several industrial, environmental, and geological concerns require a detailed understanding of barite ($BaSO_4$) growth kinetics. From an industrial standpoint, barite scale formation spontaneously occurs within geothermal wells[1] and inside fractures within geothermal reservoirs[2] (Fig. 1), which disturb both the continuous running of geothermal power plants and the efficiency of fluid circulation due to the reduction in reservoir permeability[2]. The development of new reagents that could efficiently prevent or delay the barite scale formation crucially relies on our understanding of the mechanisms of barite precipitation[3, 4].

Figure 1. Photograph of a section of 78 mm-diameter, cylindrical sandstone core (from the Buntsandstein unit) taken from the Soultz-sous-Forêts (France) EPS-1 exploration borehole, a borehole fully cored from a depth of 930 m to a depth of 2227 m in 1990-1991 (see [5-7] for information on the Soultz-sous-Forêts drilling project). The sandstone core, red/green in color, was taken from a depth of 1374 m and contains a 1-2 cm-wide fracture (in the center of the core). The fracture is partially filled with barite crystals (white in color) that have precipitated from the circulating geothermal fluids.

From an environmental standpoint, the formation of barite is known to be frequently associated with the accumulation of elevated concentrations of radionuclides such as ^{226}Ra, which has stimulated several studies dedicated to quantify the uptake of radionuclides during barite precipitation (e.g., [8-11]). Finally, from a geological standpoint, barite formation provides insight into past seawater chemistry (e.g. [12, 13]), indirectly raising the question of the mechanisms of barite precipitation from environments that contained only trace amounts of sulfate. This issue has puzzled the geochemical community for decades[14], and further emphasizes the need for a more accurate picture of the mechanisms of barite nucleation and growth[4].

In spite of the indisputable interest associated with barite formation, our knowledge regarding barite growth kinetics remains incomplete. With the noticeable exception of a few recent studies focused on barite growth on the specific (001) face over a wide range of temperatures (from 30 °C to 108 °C)[15-17], most existing studies were limited to the low temperature domain[12, 18] and were derived from experiments conducted on powders. While the resulting isotropic growth rate laws derived from powder experiments have proved useful for modeling exercises (e.g., [2]), it is noteworthy that they remain essentially empirical, which may cast doubt on their predictive ability. In particular, a recent study by Godinho and Stack[19] has shown that barite growth is an anisotropic process. Importantly, isotropic kinetic rate laws were demonstrated to be unreliable and of low relevance to model anisotropic processes such as mineral dissolution/precipitation (e.g., [19-22]), unless the same rate-limiting step controls the dissolution/growth kinetics of all faces. Among the main consequences of this anisotropic reactivity are (i) the non-uniqueness of the relation between dissolution/growth rate and the saturation state of the solution[22], (ii) the existence of a transient regime where the crystal habit continuously evolves, resulting in an equal gradual evolution of the apparent dissolution/growth rate "constant"[19, 21-24], and (iii) the existence of distinct equilibrium morphologies for a given crystal, which depend on the face-specific dissolution/growth rates of the considered crystal and therefore on reaction conditions such as temperature, fluid saturation state, and the potential catalytic / poisoning effects of

78 specific (bio)molecules[25-27]. Therefore, in addition to the expected improvement of reactive transport
79 simulations, knowledge of the variables that influence the face-specific growth rates of minerals can
80 also help decipher the factors that shape crystals, which might be useful to provide insights into the
81 putative biological origin of minerals recovered from environments on Earth and on other planets ([26]
82 and references therein).

83 To sum up, the study by Godinho and Stack[19] paved the way for a radically new description of
84 barite growth kinetics, and provided the very first data in that respect. However, their study was limited
85 to ambient temperature, whereas barite formation may occur over a wide range of environmental
86 conditions, ranging from slightly above the freezing point in oceans to several tens to hundreds of
87 degrees in geothermal reservoirs. To this end, the present study was principally aimed at extending
88 this dataset to a wider range of temperatures and to eventually derive an activation energy for face-
89 specific barite growth rate. We also provide rate data for an additional face that was not investigated
90 in the study by Godinho and Stack[19], at two different fluid saturation states. Taken together, we show
91 that the activation energy is the same for all faces (within uncertainties), which is compatible with the
92 assumption that all faces may have the same unique rate-limiting step. In addition, this activation
93 energy is close to that determined by Zhen-Wu et al.[12] for barite dissolution, which is compatible with
94 their hypothesis of micro-reversibility of barite dissolution/precipitation process.

2. Materials and methods

2.1 Starting materials and preparation

Single crystals of barite (~50-100 mm in length / diameter) were collected in Puy de Chateix (France). The chemical composition of the crystals was analyzed following the protocol described by Bracco et al.[16], revealing K, Sr and Al as the main impurities (0.14%, 0.10%, and 0.05% mol/mol Ba, respectively). The crystals were cleaved along (210) and (001) and cut along the (101) plane. The crystallographic orientations were first verified using Electron Backscatter Diffraction (EBSD) on a Tescan Vega 2 scanning electron microscope (SEM) and polished through a multi-step abrasive sequence with a final polishing step in a colloidal silica suspension. The oriented samples were divided into small pieces with a surface area (*SA*) between ~ 0.25 cm^2 and 0.50 cm^2. The faces not under study were protected with room-temperature vulcanizing (RTV) glue. For the faces under investigation, only a portion of their surface was protected with ~1 mm-diameter RTV glue spots to provide a reference surface (see similar protocol in [19, 28]). The initial roughness of each surface was measured at different scales with a ZYGO® NewView 7300 vertical scanning interferometer (VSI). For each sample, the initial average arithmetic roughness (*Ra*), defined as the arithmetic average of the absolute values of the roughness measured by the VSI, ranged between 10 and 20 nm. These initial roughness parameters were measured on 270 × 360 μm^2 VSI images.

2.2 Growth experiments and analytical procedures

Barite samples were placed over polytetrafluoroethylene (PTFE) tripods and introduced into 120 mL perfluoroalkoxy alkanes (PFA) Savillex® reactors. The reactors were filled with a volume (*V*) of 100 mL of solution and continuously stirred with magnetic bars throughout the experiments, incubated at 10, 25, 40, and 70 °C for durations ranging from 10 minutes to 15 hours. Three selected crystallographic planes were studied: (210), (001), and (101).

All solutions were prepared immediately prior to each experiment by diluting 0.01 M $BaCl_2$ and Na_2SO_4 stock solutions prepared from sodium sulfate and barium chloride powders (Acros Brand, purity ≥ 99%) to the desired concentrations. The in situ pH and ion speciation and activity were calculated using the CHESS software[29] implemented with the Debye–Hückel equation and Chess.tdb database (Lawrence Livermore National Laboratories EQ3/6 database, 8th version), and the saturation index (*SI*) with respect to barite was calculated from Eq. (1):

$$SI = \log \frac{a_{Ba} a_{SO_4}}{K_{sp}} \quad (1)$$

where a_{Ba} and a_{SO4} refer to the activities of barium and sulfate ions in solution, respectively, and K_{sp} refers to the solubility product of barite. The CHESS software calculates the solubility product at the run temperature based on the interpolation between the K_{sp} values listed in Chess.tdb database, i.e., $10^{-10.49}$, $10^{-9.97}$, $10^{-9.61}$ and $10^{-9.51}$ at 0 °C, 25 °C, 60 °C and 100 °C, respectively.

The following input solutions containing 1:1 ratio of SO_4^{2-} and Ba^{2+} activities were studied: (1) *SI* = 1.1 and (2) *SI* = 2.1. Those saturation indices were chosen in order to compare the results of this study with the growth rates obtained by Godinho and Stack[19] at room temperature.

Experiment durations ranged between 10 minutes and 15 hours, depending on the experimental conditions (*SI* and temperature). In order to calculate the evolution of the saturation index, solution sampling was carried out two to four times in each experiment. The aqueous samples were diluted 10 times and filtered using a 0.45-µm filter before analysis. Inductively coupled plasma atomic emission spectroscopy (ICP-AES - Thermo ICAP 6000) was used for the analyses of Ba^{2+} and Na^+, and ion chromatography (ICS-5000 Thermofisher Dionex) was used for the analyses of SO_4^{2-} and Cl^-. Because foreign cations such as Sr can impact barite growth rates[17], all input solutions were analyzed for major (Na, K, Ca, Mg, Fe, Si, Al) and minor (Sr, Ni, Mn, Ti, Co, Cr, Zn, Cu) cations prior to the immersion of the barite samples. The concentration of all of these elements was systematically below the detection limit (≤ 5 ppb), except for Cu, for which concentrations up to 20 ppb (8×10^{-8} M) were occasionally

detected. The pH was also checked at the beginning and at the end of each experiment. The pH of all solutions was 5.3 ± 0.1 and remained constant throughout the experiments.

At the end of each experiment, the sample was removed from the solution, rinsed with ultrapure water and sonicated for 10 min in ethanol to remove any possible secondary barite crystals nucleated from the solution and deposited on the surface, as classically done in literature to remove fine particles adhering on the surface of minerals[30]. The RTV mask was then carefully removed and the sample topography was measured with VSI in stitching mode (magnification: ×5) to evaluate average changes in height between the unreacted reference surface and the reacted mineral surface. For each surface, 10 profiles across the interface were used to calculate the average thickness of the grown layer, which was used to calculate the face-specific growth rate. The uncertainties associated with these average values were estimated from the standard deviations calculated from the various profiles. For each oriented sample, growth rates were calculated according to Eq. (2):

$$r^{(hkl)} = \frac{\Delta h}{\Delta t} \quad (2)$$

where $r^{(hkl)}$ (nm.h^{-1}) is the growth rate of the (*hkl*) face, Δh is the average surface step resulting from barite growth (nm), and Δt is the duration of the experiment (s).

3. Results and discussion

3.1 Face-specific growth patterns

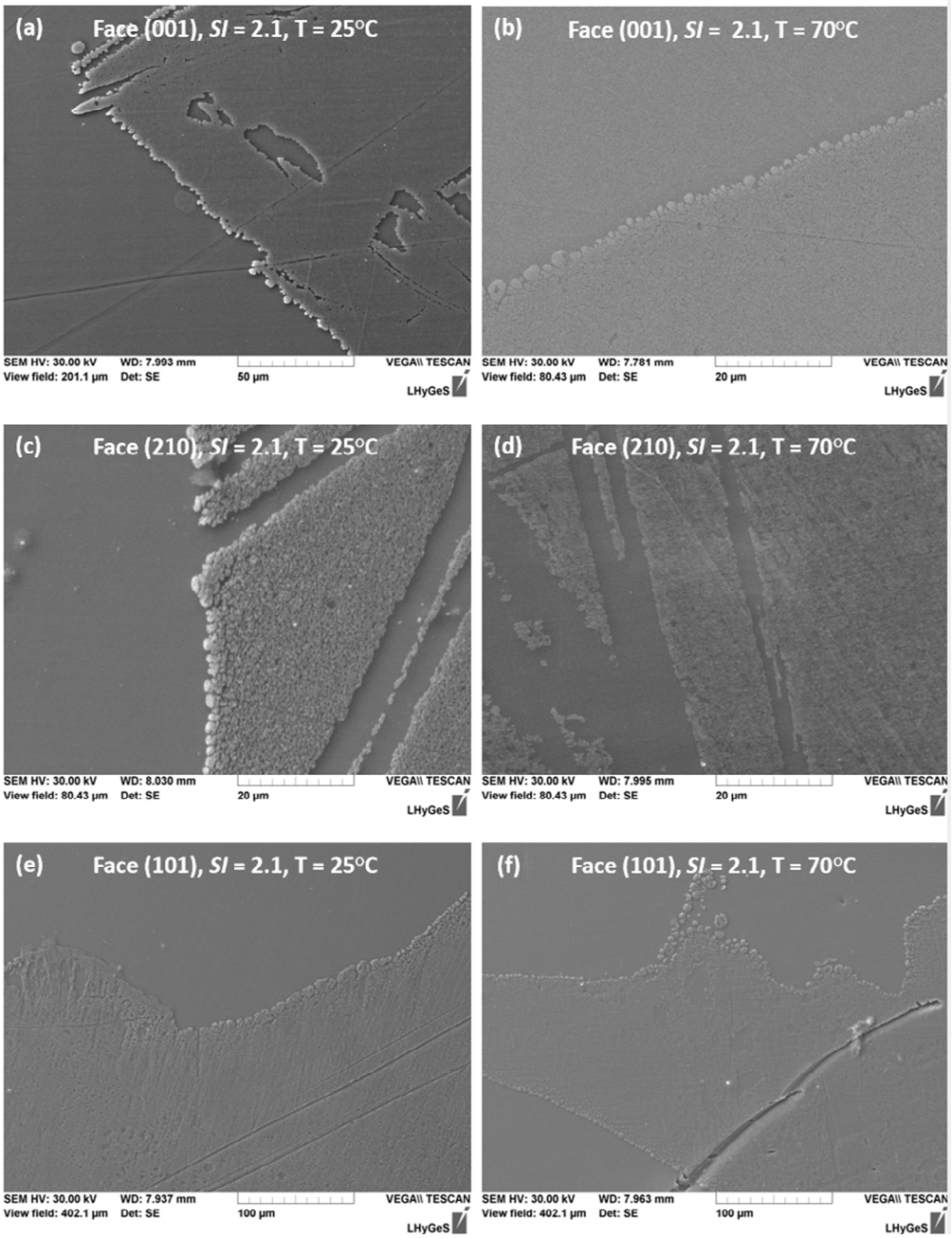

Figure 2. Barite growth features observed using scanning electron microscopy a) Face (001), *SI* = 2.1, *T* = 25 °C; b) Face (001), *SI* = 2.1, *T* = 70 °C; c) Face (210), *SI* = 2.1, *T* = 25 °C; d) Face (210), *SI* = 2.1, *T* = 70 °C; e) Face (101), *SI* = 2.1, *T* = 25 °C; f) Face (101), *SI* = 2.1, *T* = 70 °C.

Both SEM and VSI investigations confirmed that, over the course of the experiments, barite growth did not result from homogeneous nucleation in the solution, as revealed by the absence of euhedral secondary barite crystals on the surface of each investigated face, or the subsistence of polishing scratches in the grown layer of barite. The results show that the temperature variation seems to have no effect on the growth features of the faces under study. Pina et al.[31] described growth patterns which exhibit features specific to each investigated face (001) and (210), consistent with the anisotropy of the barite structure and the Periodic Bond Chain (PBC) theory. In the present study, the (001) and the (101) faces exhibit a growth morphology that resembles the circular sector shape described during the early stage of barite growth monitored using atomic force microscopy (AFM) by Sanchez-Pastor et al.[32]. Conversely, the two-dimensional islands formed in the experiments conducted at 25 and 70 ºC and a saturation index of 2.1 could not be easily related to the needle-shaped morphology described by Pina et al.[31] and Sanchez-Pastor et al.[32] for the face (210). Possible explanations include the difference of resolution between AFM and SEM, as well as the difference in terms of reaction progress, since the study by Sanchez-Pastor et al.[32] focused on the early stage of barite growth, whereas the present study reports on results obtained at a later stage of the reaction process. Therefore, part of the original islands documented in e.g. Sanchez-Pastor et al.[32] might have been overgrown, and no longer identifiable by SEM at such late stages of observation.

3.2 Face-specific growth rate of barite as a function of solution saturation state

3.2.1 Time-resolved fluid analyses

185 The evolution of the fluid composition during all experiments is provided in Table 1.
186 The Ba^{2+} to SO_4^{2-} mole ratios in the aqueous solutions are consistent with the stoichiometric
187 precipitation of barite. From the Ba^{2+}, Na^+, SO_4^{2-}, and Cl^- concentrations, the saturation index
188 with respect to barite was determined at up to four different time steps in each experiment using
189 the CHESS code.

190 The extent to which the evolution of the fluid composition resulted from barite growth
191 of the oriented barite surface sample can be estimated based on the thickness of the grown layer
192 measured by VSI following:

$$\Delta[i] = \frac{\Delta h.SA.\rho_{BaSO4}}{M_{BaSO4}.V} \quad (3)$$

193 where $\Delta[i]$ is the variation of Ba^{2+} (or SO_4^{2-}) concentration resulting from barite growth, ρ_{BaSO4}
194 and M_{BaSO4} are respectively the density (4.48 $g.cm^{-3}$) and molar mass (233 $g.mol^{-1}$) of barite.
195 Knowing that the surface area of each investigated sample never exceeded 0.5 cm^2, and using
196 150 nm as an upper bound for the thickness of the grown layer (consistent with our VSI
197 measurements), the decrease in sulfate or barite concentration should never exceed 1.5×10^{-6} M.
198 This value is about two orders of magnitude greater than the actual decrease measured in some
199 of our experiments (see Table 1), suggesting that in addition to barite growth, homogeneous
200 barite nucleation in the solution or heterogeneous nucleation on the walls of the reactor should
201 have occurred as well. This result is consistent with the observations reported by Jindra et al.[33],
202 who showed that solutions supersaturated in barite with $SI \geq 1$ were unstable with respect to
203 barite nucleation. This limitation illustrates that classical kinetics experiments based on the sole
204 evolution of the fluid composition would be poorly informative to deconvolve the nucleation
205 from the growth steps under such conditions, and further justifies the use of surface sensitive-
206 techniques to probe growth kinetics, such as AFM[15-17, 33] or VSI[19].

207 The rapid nucleation of barite complicated the conduction of experiments at a fixed
208 value of *SI*, and the duration of the experiment had consequently to be adjusted to (i) yield an

appreciable thickness of the grown layer of barite while (ii) limiting the intrinsic evolution of the solution composition resulting from barite nucleation. Importantly, for the experiments conducted under the less reactive conditions (i.e., T = 10 °C, SI = 1.1), in spite of several attempts, it has not been possible to run experiments for which the evolution of SI was modest while measuring an appreciable thickness of the grown layer at the same time. In other words, for these experiments, essentially barite nucleation occurred over short durations (with no observable grown layer), while over long durations (up to 15 hours), barite growth was observed, but with large variation of the fluid saturation index (between ± 18% and ± 34%), complicating the definition of the SI at which growth actually occurred. Therefore, the results of experiments conducted at SI = 1.1 and T = 10 °C will have to be considered with caution (see Section 3.2.2 for a confirmation of this statement). In the end, the variation of SI was ± 6% for the 12 experiments run at an initial saturation index of 2.1, and ± 5% for the 9 experiments run at SI = 1.1 (excluding the 3 experiments run at 10 °C).

Table 1. Evolution of fluid composition (concentration of Ba^{2+}, SO_4^{2-}, Cl^-, and Na^+ in mol/L) measured by ICP-AES and ion chromatography for the growth experiments realized on the (001), (101), and (210) surfaces at 10, 25, 40, and 70 ºC. The fluid composition was measured at up to four time steps in each experiment. The saturation index of the experiments was determined from the fluid composition using the CHESS software.

		SI=2.1												SI=1.1											
	face	001				210				101				001				210				101			
10°C	t	0	60	120	180	0	40	80	120	0	40	80	120	0	900			0	900			0	900		
	Ba^{2+}	8.41 *10^{-5}	7.14 *10^{-5}	6.69 *10^{-5}	4.56 *10^{-5}	7.72 *10^{-5}	6.61 *10^{-5}	5.61 *10^{-5}	5.01 *10^{-5}	7.68 *10^{-5}	6.42 *10^{-5}	6.51 *10^{-5}	5.78 *10^{-5}	4.46 *10^{-5}	2.44 *10^{-5}			3.51 *10^{-5}	2.31 *10^{-5}			3.94 *10^{-5}	2.56 *10^{-5}		
	SO_4^{2-}	1.13 *10^{-4}	1.04 *10^{-4}	9.60 *10^{-5}	9.35 *10^{-5}	1.32 *10^{-4}	1.14 *10^{-4}	1.01 *10^{-4}	9.57 *10^{-5}	1.16 *10^{-4}	9.12 *10^{-5}	9.80 *10^{-5}	8.63 *10^{-5}	5.16 *10^{-5}	3.43 *10^{-5}			4.66 *10^{-5}	3.20 *10^{-5}			4.64 *10^{-5}	3.35 *10^{-5}		
	Na^{+}	1.69 *10^{-4}	1.49 *10^{-4}	1.56 *10^{-4}	1.53 *10^{-4}	1.71 *10^{-4}	1.73 *10^{-4}	1.72 *10^{-4}	1.72 *10^{-4}	1.54 *10^{-4}	1.63 *10^{-4}	1.49 *10^{-4}	1.54 *10^{-4}	6.95 *10^{-5}	6.95 *10^{-5}			6.12 *10^{-5}	5.97 *10^{-5}			6.60 *10^{-5}	6.68 *10^{-5}		
	Cl^{-}	1.99 *10^{-4}	1.98 *10^{-4}	2.00 *10^{-4}	2.02 *10^{-4}	2.17 *10^{-4}	2.17 *10^{-4}	2.12 *10^{-4}	2.23 *10^{-4}	1.97 *10^{-4}	2.03 *10^{-4}	1.95 *10^{-4}	2.03 *10^{-4}	1.14 *10^{-4}	1.12 *10^{-4}			9.57 *10^{-5}	9.89 *10^{-5}			1.08 *10^{-4}	1.06 *10^{-4}		
	SI	**2.12**	**2.04**	**1.96**	**1.86**	**2.15**	**2.02**	**1.81**	**1.83**	**2.08**	**1.90**	**2.00**	**1.85**	**1.54**	**1.01**			**1.39**	**1.06**			**1.44**	**1.12**		
25°C	t	0	40	80	120	0	20	40	60	0	30	60	90	0	140	280	420	0	60	180	300	0	140	280	420
	Ba^{2+}	8.74 *10^{-5}	9.45 *10^{-5}	9.21 *10^{-5}	9.35 *10^{-5}	1.16 *10^{-4}	1.17 *10^{-4}	1.08 *10^{-4}	1.06 *10^{-4}	9.50 *10^{-5}	1.01 *10^{-4}	7.62 *10^{-5}	7.31 *10^{-5}	3.42 *10^{-5}	3.41 *10^{-5}	3.19 *10^{-5}	3.20 *10^{-5}	3.28 *10^{-5}	3.37 *10^{-5}	3.30 *10^{-5}	3.27 *10^{-5}	4.53 *10^{-5}	3.56 *10^{-5}	4.32 *10^{-5}	4.15 *10^{-5}
	SO_4^{2-}	1.25 *10^{-4}	1.15 *10^{-4}	1.05 *10^{-4}	9.81 *10^{-5}	1.65 *10^{-4}	1.57 *10^{-4}	1.52 *10^{-4}	1.49 *10^{-4}	1.79 *10^{-4}	1.58 *10^{-4}	1.37 *10^{-4}	1.25 *10^{-4}	4.92 *10^{-5}	4.55 *10^{-5}	4.50 *10^{-5}	4.49 *10^{-5}	3.54 *10^{-5}	3.54 *10^{-5}	3.63 *10^{-5}	3.56 *10^{-5}	5.72 *10^{-5}	5.71 *10^{-5}	5.70 *10^{-5}	5.68 *10^{-5}
	Na^{+}	1.95 *10^{-4}	1.79 *10^{-4}	1.76 *10^{-4}	1.90 *10^{-4}	1.79 *10^{-4}	1.91 *10^{-4}	1.83 *10^{-4}	1.89 *10^{-4}	1.99 *10^{-4}	1.99 *10^{-4}	2.21 *10^{-4}	1.89 *10^{-4}	7.42 *10^{-5}	7.52 *10^{-5}	7.39 *10^{-5}	7.39 *10^{-5}	6.94 *10^{-5}	7.11 *10^{-5}	7.22 *10^{-5}	7.09 *10^{-5}	8.55 *10^{-5}	8.61 *10^{-5}	8.55 *10^{-5}	8.43 *10^{-5}
	Cl^{-}	2.50 *10^{-4}	2.52 *10^{-4}	2.54 *10^{-4}	2.54 *10^{-4}	3.12 *10^{-4}	2.94 *10^{-4}	2.95 *10^{-4}	3.01 *10^{-4}	3.29 *10^{-4}	3.09 *10^{-4}	3.03 *10^{-4}	3.01 *10^{-4}	9.18 *10^{-5}	9.22 *10^{-5}	9.01 *10^{-5}	8.95 *10^{-5}	5.55 *10^{-5}	5.86 *10^{-5}	5.36 *10^{-5}	5.33 *10^{-5}	1.04 *10^{-4}	1.03 *10^{-4}	1.04 *10^{-4}	1.04 *10^{-4}
	SI	**1.90**	**1.9**	**1.88**	**1.83**	**2.13**	**2.11**	**2.06**	**2.05**	**2.07**	**2.05**	**1.89**	**1.82**	**1.13**	**1.1**	**1.06**	**1.06**	**0.98**	**0.99**	**0.99**	**0.98**	**1.32**	**1.22**	**1.3**	**1.22**
40°C	t	0	30	60	90	0	20	40	60	0	15	30	60	0	130	260	500	0	80	160	200	0	80	160	200
	Ba^{2+}	1.25 *10^{-4}	1.26 *10^{-4}	9.70 *10^{-5}	8.57 *10^{-5}	1.32 *10^{-4}	1.21 *10^{-4}	9.08 *10^{-5}	9.73 *10^{-5}	1.67 *10^{-4}	7.41 *10^{-5}	8.13 *10^{-5}		4.27 *10^{-5}	4.24 *10^{-5}	4.38 *10^{-5}	4.35 *10^{-5}	4.50 *10^{-5}	4.48 *10^{-5}	3.88 *10^{-5}	4.44 *10^{-5}	4.22 *10^{-5}	3.93 *10^{-5}	4.05 *10^{-5}	4.12 *10^{-5}
	SO_4^{2-}	1.93 *10^{-4}	1.76 *10^{-4}	1.53 *10^{-4}	1.31 *10^{-4}	2.02 *10^{-4}	1.86 *10^{-4}	1.74 *10^{-4}	1.61 *10^{-4}	2.09 *10^{-4}	1.21 *10^{-4}	1.14 *10^{-4}		5.63 *10^{-5}	5.44 *10^{-5}	5.33 *10^{-5}	5.36 *10^{-5}	4.74 *10^{-5}	4.28 *10^{-5}	4.40 *10^{-5}	4.31 *10^{-5}	4.58 *10^{-5}	4.99 *10^{-5}	4.89 *10^{-5}	5.07 *10^{-5}
	Na^{+}	2.17 *10^{-4}	2.14 *10^{-4}	2.17 *10^{-4}	2.07 *10^{-4}	2.34 *10^{-4}	2.11 *10^{-4}	2.36 *10^{-4}	2.23 *10^{-4}	2.78 *10^{-4}	2.76 *10^{-4}	2.72 *10^{-4}		8.52 *10^{-5}	8.42 *10^{-5}	8.38 *10^{-5}	8.38 *10^{-5}	1.09 *10^{-4}	8.91 *10^{-5}	9.10 *10^{-5}	9.01 *10^{-5}	8.64 *10^{-5}	9.11 *10^{-5}	9.52 *10^{-5}	9.36 *10^{-5}
	Cl^{-}	3.61 *10^{-4}	3.60 *10^{-4}	3.63 *10^{-4}	3.92 *10^{-4}	3.55 *10^{-4}	3.47 *10^{-4}	3.56 *10^{-4}	3.55 *10^{-4}	4.37 *10^{-4}	4.35 *10^{-4}	4.34 *10^{-4}		1.07 *10^{-4}	1.05 *10^{-4}	1.04 *10^{-4}	1.04 *10^{-4}	7.36 *10^{-5}	7.43 *10^{-5}	7.12 *10^{-5}	7.49 *10^{-5}	8.24 *10^{-5}	8.96 *10^{-5}	7.40 *10^{-5}	7.31 *10^{-5}
	SI	**2.02**	**1.99**	**1.87**	**1.7**	**2.06**	**1.99**	**1.84**	**1.84**	**2.17**	**1.6**	**1.62**		**1.08**	**1.07**	**1.07**	**1.07**	**1.04**	**1.00**	**0.95**	**0.99**	**1.00**	**1.00**	**1.01**	**1.03**
70°C	t	0	5	10		0	5	10		0	5	10		0	60	120		0	60	120	180	0	40	80	120
	Ba^{2+}	1.91 *10^{-4}	1.86 *10^{-4}	1.38 *10^{-4}		1.86 *10^{-4}	1.63 *10^{-4}	1.37 *10^{-4}		1.95 *10^{-4}	1.56 *10^{-4}	1.25 *10^{-4}		6.32 *10^{-5}	4.88 *10^{-5}	3.71 *10^{-5}		6.04 *10^{-5}	5.68 *10^{-5}	5.09 *10^{-5}	4.64 *10^{-5}	6.32 *10^{-5}	3.95 *10^{-5}	5.74 *10^{-5}	5.81 *10^{-5}
	SO_4^{2-}	2.00 *10^{-4}	1.88 *10^{-4}	1.47 *10		2.21 *10^{-4}	1.95 *10^{-4}	1.78 *10^{-4}		2.73 *10^{-4}	2.08 *10^{-4}	1.64 *10^{-4}		9.83 *10^{-5}	8.00 *10^{-5}	7.67 *10^{-5}		9.26 *10^{-5}	8.65 *10^{-5}	8.24 *10^{-5}	7.39 *10^{-5}	6.74 *10^{-5}	6.78 *10^{-5}	6.74 *10^{-5}	6.53 *10^{-5}
	Na^{+}	3.97 *10^{-4}	4.00 *10^{-4}	4.02 *10^{-4}		4.07 *10^{-4}	4.10 *10^{-4}	5.1 *10^{-4}		4.07 *10^{-4}	3.73 *10^{-4}	3.73 *10^{-4}		1.84 *10^{-4}	1.71 *10^{-4}	1.83 *10^{-4}		9.84 *10^{-5}	1.07 *10^{-4}	1.09 *10^{-4}	9.90 *10^{-5}	1.33 *10^{-4}	1.38 *10^{-4}	1.34 *10^{-4}	1.34 *10^{-4}
	Cl^{-}	4.20 *10^{-4}	4.06 *10^{-4}	4.10 *10^{-4}		3.96 *10^{-4}	3.95 *10^{-4}	4.95 *10^{-4}		5.81 *10^{-4}	5.80 *10^{-4}	5.97 *10^{-4}		1.88 *10^{-4}	1.95 *10^{-4}	1.98 *10^{-4}		1.36 *10^{-4}	1.37 *10^{-4}	1.41 *10^{-4}	1.34 *10^{-4}	1.19 *10^{-4}	1.16 *10^{-4}	1.16 *10^{-4}	1.17 *10^{-4}
	SI	**2.00**	**1.97**	**1.74**		**2.03**	**1.93**	**1.81**		**2.1**		**1.7**		**1.25**	**1.14**	**0.92**		**1.21**	**1.16**	**1.1**	**1.0**	**1.11**	**0.91**	**1.07**	**1.06**

228

3.2.2 Vertical Scanning Interferometry data:

Table 2. Face-specific growth rates ($nm.h^{-1}$) calculated from the thickness of the grown layer measured by VSI on the (001), (101), and (210) surfaces of crystals grown in two different solutions: (1) *SI* = 1.1 and (2) *SI* = 2.1. Experiments were performed at 10, 25, 40, and 70 °C. The numbers between parentheses indicate the uncertainties of the growth rates, estimated from the variability of the thickness of the grown layer averaged on 10 measurements (see Section 2.2).

(1) SI = 1.1				
Face		(0 0 1)		
T (°C)	10	25	40	70
r (nm/h)	0.60 (0.07)	5.1 (0.5)	19.9 (1.3)	38.7 (4.2)
Face		(2 1 0)		
T (°C)	10	25	40	70
r (nm/h)	1.4 (0.7)	4.4 (0.7)	10.7 (1.3)	46.9 (1.2)
Face		(1 0 1)		
T (°C)	10	25	40	70
r (nm/h)	2.3 (0.3)	6.8 (2.8)	8.9 (0.8)	37.6 (4.9)
(2) SI = 2.1				
Face		(0 0 1)		
T (°C)	10	25	40	70
r (nm/h)	25.0 (6.3)	46.1 (14.9)	96.6 (8.9)	318 (38)
Face		(2 1 0)		
T (°C)	10	25	40	70
r (nm/h)	39.0 (4.4)	86.2 (4.7)	125 (18)	296 (27)
Face		(1 0 1)		
T (°C)	10	25	40	70
r (nm/h)	25.5 (4.2)	82.7 (9.1)	131 (15)	285 (71)

The growth rates perpendicular to the three studied surfaces were calculated from the measured thickness of the layer grown whilst in solution. The results highlight an effect of the saturation index on growth rate. For example, in the experiments with a starting saturation index of 2.1, the growth rates are about 5 to 40 times faster (depending on the face and temperature) than in the solution with *SI* = 1.1 (Table 1).

Surface-controlled precipitation rates are commonly fitted to the following rate law (e.g. [34] and references therein):

$$r = k.(10^{SI} - 1)^n \quad (4)$$

where k is the growth rate constant and n is a fitting coefficient generally referred to as the reaction order. Although Eq. (4) essentially remains empirical, the value of the reaction order is usually attributed to the rate-controlling reaction mechanism (a reaction order of 1 is typically attributed to a

simple surface adsorption mechanism and a reaction order of 2 to spiral growth; see [35]). For each face, the value of the reaction order at each temperature (n_T) can therefore be estimated following:

$$n_T = \frac{\log r_2^T - \log r_1^T}{\log\left(10^{SI_2^T} - 1\right) - \log\left(10^{SI_1^T} - 1\right)} \quad (5)$$

where r_i^T refers to the growth rate measured at the corresponding saturation index SI_i^T (i.e., ~2.1 or ~1.1), for a given temperature *T*. Eq. (5) was used to estimate the value of *n* for each face and all investigated temperatures (Table 3), leading to average values of *n* = 1.39 ± 0.76, 1.26 ± 0.42, and 1.12 ± 0.19 for the (001), (210), and (101) faces, respectively. Of note, the large standard deviations associated with the value of *n* for the (001) and (210) faces are essentially due to the value of *n* derived for these faces at 10 °C (*n* = 2.50 and 1.88, respectively). The large uncertainties associated with the estimation of slow growth rates at low temperature and saturation index may partially contribute to this observation, as emphasized above (Section 3.2.1). In particular, the large variation of *SI* over the duration of these experiments, which result from the fact that barite precipitation occurred almost exclusively through homogeneous nucleation, considerably complicated the definition of the value of *SI* at which barite growth occurred. Therefore, the uncertainties associated with these experiments and the switch in barite precipitation mechanism at low temperature justifies the need to remove the rate data collected at 10 °C and *SI* = 1.1 for further processing of the dataset . If these rates are discarded from the dataset, the average values then become *n* = 1.02 ± 0.19; 1.05 ± 0.07 and 1.11 ± 0.13 for the (001), (210) and (101) faces, respectively. Therefore, with the noticeable exception of rate data obtained at 10 °C, our results show that a simple linear relation between *r* and (10^{SI} – 1) can account for our observations for all faces, irrespective of the temperature (see Supporting Information for a plot displaying the general agreement over the whole dataset). Therefore, this study extends the similar conclusion previously reached by Zhen-Wu et al. [12] from powder experiments to a broader range of temperatures and saturation indices, while suggesting that the reaction order (*n*) does not depend on the investigated face, at least for temperatures ranging from 25 °C to 70 °C. This result is also

consistent with the second order reaction with respect to Ba concentration reported by Christy and Putnis[18], since a first order reaction with respect to barite saturation state is equivalent to a second order reaction with respect to either aqueous barium or aqueous sulfate concentration, as recalled by Zhen-Wu et al.[12].

Table 3. Estimation of the reaction order (n) of barite growth kinetics for all investigated faces and temperatures following Eq. (5). Note that the values in italic were not considered for the calculation of the mean value of n for each face. See text for details.

	10 °C	**25 °C**	**40 °C**	**70 °C**
(0 0 1)	*2.50*	1.16	0.80	1.10
(2 1 0)	*1.88*	1.11	1.06	0.97
(1 0 1)	*1.14*	1.37	1.04	0.92

3.3 Face-specific growth rate of barite as a function of temperature

In experiments conducted with an input solution with SI = 1.1, growth rates range from 0.60 nm.h^{-1} to approximately 47 nm.h^{-1}, with the slowest rates at 10ºC and the fastest rates at 70 ºC (Table 1). For each face, the growth rate increases with temperature but generally, the (001) and (101) faces are the slowest growing faces (Table 1), in accordance with the results obtained by Godinho and Stack[19]. For face (001) reacted in a solution with SI = 1.1, an increase in temperature by 60 ºC increases the rate by almost a factor of 60 (Table 1). At a starting saturation index of 2.1, the growth rates are about one order of magnitude greater at 70 °C than at 10 °C for all faces.

The dependence of the mineral growth rate constant on temperature is usually described following the Arrhenius equation:

$$k = A.\exp(-E_a/RT) \quad (6)$$

where A represents the Arrhenius pre-exponential factor, E_a denotes the activation energy, R is the gas constant, and T refers to the absolute temperature. By combining Eq. (6) with Eq. (4) and assuming that n = 1 (see above), we can determine the value of A and E_a experimentally following the relation:

$$\ln(r/(10^{SI}-1)) = \ln A - E_a/RT \quad (7)$$

This equation was applied to the data generated in this study using the Arrhenius plots shown in Fig. 3. The errors reported on the data points account both for the uncertainties on the growth rates (resulting from the variability of the thickness of the grown layer) and the variation of *SI* over the course of the experiment (resulting from the precipitation of barite). Excluding the rate data obtained at 10 °C and *SI* = 1.1 (see above), the activation energy was found to be virtually independent of the considered face, with values of 36.4 ± 4.0, 31.8 ± 3.3, and 35.8 ± 3.7 kJ.mol^{-1} for the growth on (001), (210), and (101) faces, respectively. The uncertainties on the activation energies were determined based on the errors associated with the data depicted in Fig. 3.

The activation energy determined for the growth on the (001) face is in excellent agreement with that determined by Higgins et al.[36] (37.3 ± 4.6 kJ.mol^{-1}). More broadly, these values agree, within uncertainties, with those reported by Christy and Putnis[18] (22.0 ± 14.3 kJ.mol^{-1}) for the growth of barite monitored on powder experiments over the temperature range 44-85 °C. This result further indicates that if a barite crystal form is developed based on the three faces investigated in the present study, the morphology of barite crystals will be negligibly affected by temperature variations, such that the morphology of barite crystals cannot be used as a criterion to determine the temperature at which they crystallized.

Regarding the pre-exponential factor, Fig. 3 reveals that it only slightly varies with the considered orientation, from exp(12.4) nm.h^{-1} for the (210) face to exp(14.1) nm.h^{-1} for the (001) face. Following the reasonable assumption that the activation energy does not depend on the crystallographic orientation for the three investigated faces, this translates into a modest anisotropy of barite growth rate of a ~5-fold factor between the fastest and slowest growing faces, which is in reasonable agreement with our experimental data.

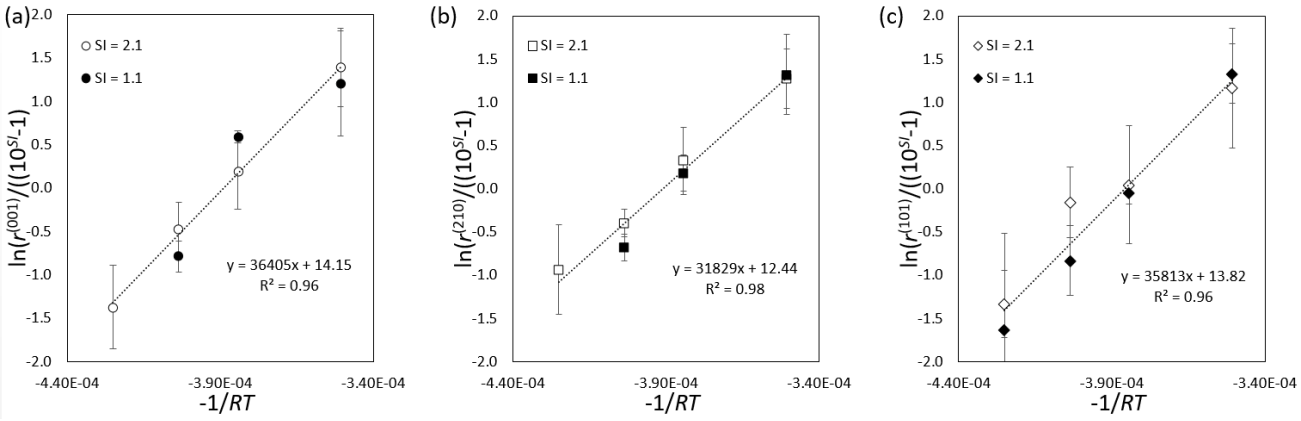

Figure 3. Determination of the face-specific activation energy ($E_a^{(hkl)}$) and pre-exponential factor ($A^{(hkl)}$) of barite growth rate over the temperature range 10-70 °C for the (a) (001), (b) (210), and (c) (101) faces. Of note, the rate data obtained at 10 °C and SI = 1.1 for the faces (001) and (210) were dismissed from the regressions (see section 3.3 for details).

The agreement between the multiple regressions described above and the experimental data can be assessed in Fig. 4, for growth rates varying over about two orders of magnitude. In Fig. 4a, the measured rates were compared with the corresponding values calculated following the overall face-specific growth rate law given by:

$$r^{(hkl)} = A^{(hkl)}.\exp\left(-E_a^{(hkl)}/RT\right).(10^{SI} - 1) \quad (8a)$$

for which the values of $A^{(hkl)}$ and $E_a^{(hkl)}$ were derived from the plots depicted in Fig. 3. Of note, the agreement between calculated rates and measured rate data is negligibly affected if one considers an overall isotropic growth rate law for all faces following:

$$r^{(hkl)} = A.\exp(-E_a/RT).(10^{SI} - 1) \quad (8b)$$

with average values of A = exp (13.59) nm.h^{-1} and E_a = 35.0 ± 2.5 kJ.mol^{-1} (Fig. 4b). In addition, both rate laws perfectly account for the rate data reported by Godinho and Stack[19] at T = 22.2 °C and SI = 2.1 for the faces (001) and (210), while overestimating the rate values obtained at SI = 1.1. Possible explanations might reside in the difference in chemical composition of the crystals used to conduct the studies, since impurities such as strontium are known to decrease barite growth rates at low concentrations[17].

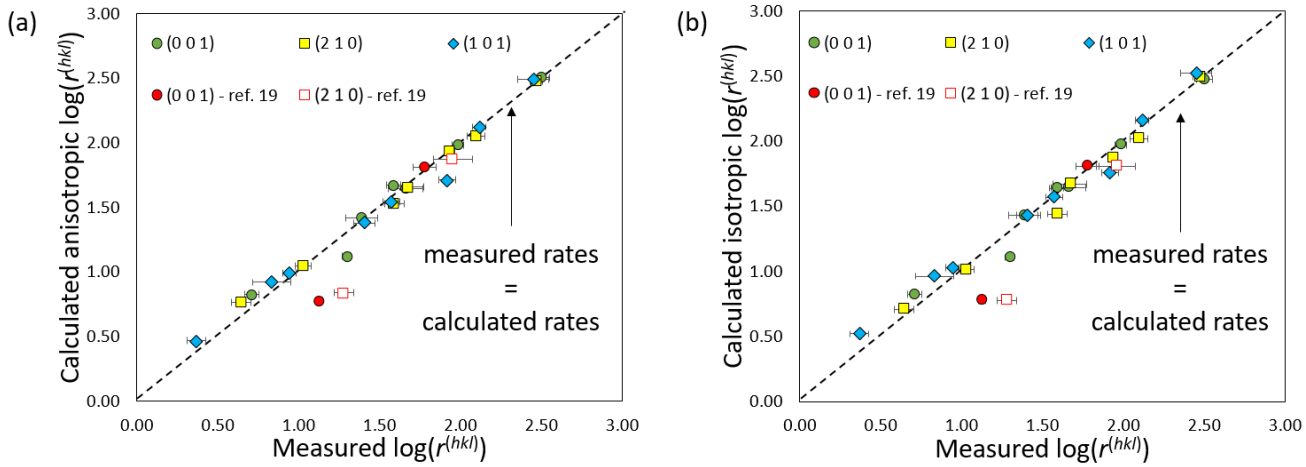

Figure 4. Comparison of barite growth rates calculated using (a) Eq. (8a) or (b) Eq. (8b) with those measured in the present study or reported in Godinho and Stack[19].

3.4 Comparison with previously published data and mechanistic insights

Overall, this study largely confirms both the measurements of face-specific barite growth rates and the reaction mechanisms reported in previous studies.

Regarding the anisotropy of barite growth, Godinho and Stack[19] reported that the reactivity of the (210) face was about 1.5 times greater than that of the (001) face at ambient temperature and for *SI* conditions ranging from 1.1 to 2.1. These values are in excellent agreement with our measurements under the same conditions, which show that the reactivity of the (210) face is approximately between 1.7 and 1.9 times greater than that of the (001) face. At $SI = 2.1$, the absolute values of the growth rates of the two studies overlap as well, within uncertainties.

Regarding the reaction mechanisms, several lines of evidence suggest that barite growth may observe the principle of detailed balancing and micro-reversibility. First, our rate data are consistent with an isotropic activation energy with an average value of 35.0 ± 2.5 kJ.mol^{-1}, suggesting that the reaction is surface-controlled. Moreover, if the rate-limiting step of barite growth were to change with surface orientation, then the activation energies of barite growth rate would be face-specific. Therefore,

and even though the activation energies estimated in the present study remain essentially apparent, the unicity of the activation energy is compatible with the suggestion that the same elementary step is rate-limiting for all faces. In addition, this value is consistent with the isotropic value reported by Christy and Putnis[18] (22.0 ± 14.3 kJ.mol^{-1}), itself very similar to the activation energy of barite dissolution reported by Zhen-Wu et al.[12] (25 ± 2 kJ.mol^{-1}). Second, the growth rate was found to be a linear function of the saturation state of the solution (i.e., $r \propto 10^{SI}$) for all faces at temperatures ranging between 25 and 70 °C (this statement remains questionable at lower temperatures). This result is consistent with previously published studies[12, 18] and is typical of adsorption-controlled growth processes[35], for which the concept of micro-reversibility necessarily applies.

3.5 Implications for natural and anthropogenic systems

As highlighted above, a growing number of studies have emphasized the need to go beyond the classical development of isotropic rate laws to model the dissolution and/or the growth kinetics of minerals, partly because of their anisotropic reactivity. Notwithstanding, switching to more complex rate laws that are not implemented so far in classical reactive transport codes has to be justified through quantitative measurements of this anisotropy, as well as its dependence to fundamental rate-controlling parameters such as temperature or solution saturation state, in order to assess the extent to which isotropic models fail to reproduce quantitatively the actual mineral reactivity. In that respect, our results underline that (i) the anisotropic reactivity of barite growth remains modest, at least for the three studied faces and (ii) the growth activation energy is similar for all faces and possibly equivalent to the dissolution activation energy. These results have at least two practical implications for natural and anthropogenic systems:

(i) Regarding the reaction mechanisms, our study suggests that the principle of detailed balancing may be respected over the range of *T* and *SI* investigated in the present study (see section 3.4). Because the dissolution and precipitation rates of barite are relatively rapid, this result implies

that at ambient temperature and close-to-equilibrium conditions, the isotope composition of barium may be quickly reset, consistent with the results of Curti et al.[8]. Because the isotopic and elemental compositions of barite are used as a proxy for past seawater chemistry ([12] and references therein), our study contributes to the general warning regarding the preservation of isotopic signatures in minerals over geological timescales to trace paleoenvironmental conditions[37-40].

(ii) Regarding geothermal systems, a viable geothermal resource requires a reservoir with a high permeability, often provided by fractures (e.g., [41]), to provide the flow rates required for efficient energy production. The hydrothermal brines circulating through these reservoirs typically contain a rich assortment of dissolved elements (e.g., [41-44]) that can precipitate in surface installations and within permeability-enhancing fractures within the reservoir as a result of, for example, changes in temperature (e.g., [2]). Barite scaling can play havoc at geothermal surface installations, requiring time-consuming and expensive mechanical removal (e.g., [18]), and can dramatically reduce the permeability of fractures within the reservoir. For example, Griffiths et al.[2] highlighted that the Buntsandstein unit, a ~400 m-thick unit of sandstone that directly overlies the granitic reservoir at geothermal sites throughout the Upper Rhine Graben (e.g., [45-47]), contains abundant barite-filled fractures (e.g., Fig. 1). Additionally, Griffiths et al.[2] estimated the time needed to seal a 2 mm-wide fracture with barite to be on the order of about a month. These calculations, however, were performed using data collected on powdered barite samples[18]. Our new face-specific data show that the activation energy is, within uncertainty, the same for all of the studied crystal faces. These new data provide additional confidence in the barite growth timescales provided in Griffiths et al.[2], which suggest that the permeability of the geothermal reservoir adjacent to the injection well could be, unless preventative measures are taken, greatly reduced over short timescales during production.

4. Summary and conclusions

Barite growth experiments combined with vertical scanning interferometry measurements of the surface topography have been conducted to study the effect of the saturation index (*SI*) and the temperature on the growth rates and surface features of the (001), (210), and (101) faces of barite. The results confirmed that barite growth is anisotropic with a rate that is promoted by elevated saturation indices and temperatures, while the growth morphologies observed by scanning electron microscopy did not significantly vary with temperature or *SI*. It was determined that barite growth rate observes a first order reaction with respect to barite saturation state for all faces at all temperatures, with the exception of rate data obtained at 10 °C. Therefore, our results show that a simple linear relation between r and $(10^{SI} - 1)$ can account for barite growth. From the dependence of the rate of barite growth with temperature, the activation energy could be defined for each face using the Arrhenius equation, yielding an average value of 35.0 ± 2.5 kJ.mol^{-1}, with no significant difference between the three faces. This result indicates that the morphology of barite crystals will be negligibly affected by temperature variations for a crystal composed of the faces under study. Therefore, the morphology of barite crystals cannot be used as a criterion to determine the temperature at which they crystallized. These data are also compatible with a reaction rate is surface-controlled, with the same rate-limiting step for all faces. The pre-exponential factor in the Arrhenius equation slightly varies with the considered orientation, from exp(12.4) nm.h^{-1} for the (210) face to exp(14.1) nm.h^{-1} for the (001) face, which represents a modest anisotropy of barite growth rate. Taken together, this study largely confirms both the measurements of face-specific barite growth rates and the reaction mechanisms reported in previous studies, and may contribute to improve modeling of barite growth rates in natural and anthropogenic systems.

Acknowledgements

This study was partly funded by LABEX grant ANR-11-LABX-0050_G-EAU-THERMIE-PROFONDE (this research therefore benefited from state funding managed by the Agence National de la Recherche (ANR) as part of the "Investissements d'avenir" program) and ANR grant CANTARE (ANR-15-CE06-0014-01). The authors are grateful to the National Scientific and Technical Research Council (CONICET) PIP2011-0392 which provided a post-doctoral grant. We also acknowledge the Mincyt-ECOS project for supporting international collaboration between the ICGyC/IIMyC in Argentina and the LHyGeS in France. Colin Fourtet and René Boutin (LHyGeS) are warmly thanked for their help with IC and ICP-AES measurements. Finally, we are grateful for the careful reviews and detailed suggestions made by two anonymous reviewers, which significantly improved an earlier version of the present paper.

Supporting information

Additional data processing and graph illustrating the linear relation between barite growth rates and the saturation state of the solution.

References

(1) Bozau, E.; Häußler, S.; van Berk, W. Hydrogeochemical modelling of corrosion effects and barite scaling in deep geothermal wells of the North German Basin using PHREEQC and PHAST. *Geothermics* **2015,** *53*, 540-547.

(2) Griffiths, L.; Heap, M. J.; Wang, F.; Daval, D.; Gilg, H. A.; Baud, P.; Schmittbuhl, J.; Genter, A. Geothermal implications for fracture-filling hydrothermal precipitation. *Geothermics* **2016,** *64*, 235-245.

(3) Ruiz-Agudo, C.; Putnis, C. V.; Putnis, A. The effect of a copolymer inhibitor on baryte precipitation. *Mineral. Mag.* **2014,** *78*, 1423-1430.

(4) Ruiz-Agudo, C.; Ruiz-Agudo, E.; Putnis, C. V.; Putnis, A. Mechanistic Principles of Barite Formation: From Nanoparticles to Micron-Sized Crystals. *Cryst. Growth Des.* **2015,** *15*, 3724-3733.
(5) Gérard, A.; Kappelmeyer, O. The Soultz-sous-Forêts project. *Geothermics* **1987,** *16*, 393-399.
(6) Baria, R.; Baumgärtner, J.; Gérard, A.; Jung, R.; Garnish, J. European HDR research programme at Soultz-sous-Forêts (France) 1987–1996. *Geothermics* **1999,** *28*, 655-669.
(7) Gérard, A.; Genter, A.; Kohl, T.; Lutz, P.; Rose, P. The deep EGS (enhanced geothermal system) project at Soultz-sous-Forêts (Alsace, France). *Geothermics* **2006,** *35*, 473-483.
(8) Curti, E.; Fujiwara, K.; Iijima, K.; Tits, J.; Cuesta, C.; Kitamura, A.; Glaus, M. A.; Müller, W. Radium uptake during barite recrystallization at 23±2°C as a function of solution composition: An experimental 133Ba and 226Ra tracer study. *Geochim. Cosmochim. Acta* **2010,** *74*, 3553-3570.
(9) Rosenberg, Y. O.; Sadeh, Y.; Metz, V.; Pina, C. M.; Ganor, J. Nucleation and growth kinetics of RaxBa1− xSO4 solid solution in NaCl aqueous solutions. *Geochim. Cosmochim. Acta* **2014,** *125*, 290-307.
(10) Klinkenberg, M.; Brandt, F.; Breuer, U.; Bosbach, D. Uptake of Ra during the recrystallization of barite: a microscopic and time of flight-secondary ion mass spectrometry study. *Environ. Sci. Technol.* **2014,** *48*, 6620-6627.
(11) Brandt, F.; Curti, E.; Klinkenberg, M.; Rozov, K.; Bosbach, D. Replacement of barite by a (Ba, Ra) SO4 solid solution at close-to-equilibrium conditions: A combined experimental and theoretical study. *Geochim. Cosmochim. Acta* **2015,** *155*, 1-15.
(12) Zhen-Wu, B. Y.; Dideriksen, K.; Olsson, J.; Raahauge, P. J.; Stipp, S. L. S.; Oelkers, E. H. Experimental determination of barite dissolution and precipitation rates as a function of temperature and aqueous fluid composition. *Geochim. Cosmochim. Acta* **2016,** *194*, 193-210.
(13) Gonzalez-Muñoz, M.; Martinez-Ruiz, F.; Morcillo, F.; Martin-Ramos, J.; Paytan, A. Precipitation of barite by marine bacteria: a possible mechanism for marine barite formation. *Geology* **2012,** *40*, 675-678.
(14) McGrail, B. P.; Schaef, H. T.; Spane, F. A.; Cliff, J. B.; Qafoku, O.; Horner, J. A.; Thompson, C. J.; Owen, A. T.; Sullivan, C. E. Field Validation of Supercritical CO2 Reactivity with Basalts. *Environ. Sci. Technol. Lett.* **2017,** *4*, 6-10.
(15) Kuwahara, Y.; Liu, W.; Makio, M.; Otsuka, K. In Situ AFM Study of Crystal Growth on a Barite (001) Surface in BaSO4 Solutions at 30° C. *Minerals* **2016,** *6*, 117.
(16) Bracco, J. N.; Gooijer, Y.; Higgins, S. R. Hydrothermal atomic force microscopy observations of barite step growth rates as a function of the aqueous barium-to-sulfate ratio. *Geochim. Cosmochim. Acta* **2016,** *183*, 1-13.
(17) Weber, J.; Bracco, J. N.; Poplawsky, J. D.; Ievlev, A. V.; More, K. L.; Lorenz, M.; Bertagni, A. L.; Jindra, S. A.; Starchenko, V.; Higgins, S. R.; Stack, A. G. Unraveling the Effects of Strontium Incorporation on Barite Growth—In Situ and Ex Situ Observations Using Multiscale Chemical Imaging. *Cryst. Growth Des.* **2018,** *18*, 5521-5533.
(18) Christy, A. G.; Putnis, A. The kinetics of barite dissolution and precipitation in water and sodium chloride brines at 44–85°C. *Geochim. Cosmochim. Acta* **1993,** *57*, 2161-2168.
(19) Godinho, J. R. A.; Stack, A. G. Growth Kinetics and Morphology of Barite Crystals Derived from Face-Specific Growth Rates. *Cryst. Growth Des.* **2015,** *15*, 2064-2071.
(20) Daval, D.; Hellmann, R.; Saldi, G. D.; Wirth, R.; Knauss, K. G. Linking nm-scale measurements of the anisotropy of silicate surface reactivity to macroscopic dissolution rate laws: New insights based on diopside. *Geochim. Cosmochim. Acta* **2013,** *107*, 121-134.
(21) Godinho, J. R.; Piazolo, S.; Evans, L. Simulation of surface dynamics during dissolution as a function of the surface orientation: Implications for non-constant dissolution rates. *Earth Planet. Sci. Lett.* **2014,** *408*, 163-170.
(22) Pollet-Villard, M.; Daval, D.; Ackerer, P.; Saldi, G. D.; Wild, B.; Knauss, K. G.; Fritz, B. Does crystallographic anisotropy prevent the conventional treatment of aqueous mineral reactivity? A case study based on K-feldspar dissolution kinetics. *Geochim. Cosmochim. Acta* **2016,** *190*, 294-308.

(23) Briese, L.; Arvidson, R. S.; Luttge, A. The effect of crystal size variation on the rate of dissolution – A kinetic Monte Carlo study. *Geochim. Cosmochim. Acta* **2017,** *212*, 167-175.
(24) Robin, V.; Wild, B.; Daval, D.; Pollet-Villard, M.; Nonat, A.; Nicoleau, L. Experimental study and numerical simulation of the dissolution anisotropy of tricalcium silicate. *Chem. Geol.* **2018,** *497*, 64-73.
(25) Montes-Hernandez, G.; Fernandez-Martinez, A.; Charlet, L.; Renard, F.; Scheinost, A. C.; Bueno, M. Synthesis of a Se-0/calcite composite using hydrothermal carbonation of Ca(OH)(2) coupled to a complex selenocystine fragmentation. *Cryst. Growth Des.* **2008,** *8*, 2497-2504.
(26) Benzerara, K.; Menguy, N. Looking for traces of life in minerals. *CR Palevol* **2009,** *8*, 617-628.
(27) Guisbiers, G.; José-Yacaman, M. Use of chemical functionalities to control stability of nanoparticles. *Reference Module in Chemistry, Molecular Sciences and Chemical Engineering* **2017**.
(28) Wild, B.; Daval, D.; Guyot, F.; Knauss, K. G.; Pollet-Villard, M.; Imfeld, G. pH-dependent control of feldspar dissolution rate by altered surface layers. *Chem. Geol.* **2016,** *442*, 148-159.
(29) van der Lee, J.; De Windt, L., *CHESS Tutorial and Cookbook. Updated for version 3.0.* ed.; Paris, 2002; Vol. Manual Nr. LHM/RD/02/13, p 116.
(30) Schott, J.; Berner, R. A.; Lennart Sjöberg, E. Mechanism of pyroxene and amphibole weathering--I. Experimental studies of iron-free minerals. *Geochim. Cosmochim. Acta* **1981,** *45*, 2123-2135.
(31) Pina, C. M.; Becker, U.; Risthaus, P.; Bosbach, D.; Putnis, A. Molecular-scale mechanisms of crystal growth in barite. *Nature* **1998,** *395*, 483-486.
(32) Sánchez-Pastor, N.; Pina, C. M.; Fernández-Díaz, L.; Astilleros, J. M. The effect of CO_3^{2-} on the growth of barite {0 0 1} and {2 1 0} surfaces: An AFM study. *Surf. Sci.* **2006,** *600*, 1369-1381.
(33) Jindra, S. A.; Bertagni, A. L.; Bracco, J. N.; Higgins, S. R. Hydrothermal Atomic Force Microscopy Investigation of Barite Growth: Role of Spectator Ions in Elementary Step Edge Growth Kinetics and Hillock Morphology. *Cryst. Growth Des.* **2017,** *17*, 6085-6095.
(34) Lopez, O.; Zuddas, P.; Faivre, D. The influence of temperature and seawater composition on calcite crystal growth mechanisms and kinetics: Implications for Mg incorporation in calcite lattice. *Geochim. Cosmochim. Acta* **2009,** 73, 337-347.
(35) Shiraki, R.; Brantley, S. L. Kinetics of near-equilibrium calcite precipitation at 100°C: An evaluation of elementary reaction-based and affinity-based rate laws. *Geochim. Cosmochim. Acta* **1995,** *59*, 1457-1471.
(36) Higgins, S. R.; Bosbach, D.; Eggleston, C. M.; Knauss, K. G. Kink Dynamics and Step Growth on Barium Sulfate (001): A Hydrothermal Scanning Probe Microscopy Study. *J. Phys. Chem. B* **2000,** 104, 6978-6982.
(37) Critelli, T.; Marini, L.; Schott, J.; Mavromatis, V.; Apollaro, C.; Rinder, T.; De Rosa, R.; Oelkers, E. Dissolution rate of antigorite from a whole-rock experimental study of serpentinite dissolution from 2< pH< 9 at 25 C: Implications for carbon mitigation via enhanced serpentinite weathering. *Appl. Geochem.* **2015,** *61*, 259-271.
(38) Bernard, S.; Daval, D.; Ackerer, P.; Pont, S.; Meibom, A. Burial-induced oxygen-isotope re-equilibration of fossil foraminifera explains ocean paleotemperature paradoxes. *Nat. Commun.* **2017,** *8*, 1134.
(39) Chanda, P.; Gorski, C. A.; Oakes, R. L.; Fantle, M. S. Low temperature stable mineral recrystallization of foraminiferal tests and implications for the fidelity of geochemical proxies. *Earth Planet. Sci. Lett.* **2019,** *506*, 428-440.
(40) Oelkers, E. H.; Pogge von Strandmann, P. A. E.; Mavromatis, V. The rapid resetting of the Ca isotopic signatures of calcite at ambient temperature during its congruent dissolution, precipitation, and at equilibrium. *Chem. Geol.* **2019,** *512*, 1-10.

(41) Kushnir, A. R.; Heap, M. J.; Baud, P. Assessing the role of fractures on the permeability of the Permo-Triassic sandstones at the Soultz-sous-Forêts (France) geothermal site. *Geothermics* **2018,** *74*, 181-189.
(42) Aquilina, L.; Pauwels, H.; Genter, A.; Fouillac, C. Water-rock interaction processes in the Triassic sandstone and the granitic basement of the Rhine Graben: Geochemical investigation of a geothermal reservoir. *Geochim. Cosmochim. Acta* **1997,** *61*, 4281-4295.
(43) Sanjuan, B.; Millot, R.; Dezayes, C.; Brach, M. Main characteristics of the deep geothermal brine (5km) at Soultz-sous-Forêts (France) determined using geochemical and tracer test data. *C. R. Geosci.* **2010,** *342*, 546-559.
(44) Sanjuan, B.; Millot, R.; Innocent, C.; Dezayes, C.; Scheiber, J.; Brach, M. Major geochemical characteristics of geothermal brines from the Upper Rhine Graben granitic basement with constraints on temperature and circulation. *Chem. Geol.* **2016,** *428*, 27-47.
(45) Aichholzer, C.; Duringer, P.; Orciani, S.; Genter, A. New stratigraphic interpretation of the Soultz-sous-Forêts 30-year-old geothermal wells calibrated on the recent one from Rittershoffen (Upper Rhine Graben, France). *Geotherm. Energy* **2016,** *4*, 13.
(46) Heap, M. J.; Kushnir, A. R.; Gilg, H. A.; Wadsworth, F. B.; Reuschlé, T.; Baud, P. Microstructural and petrophysical properties of the Permo-Triassic sandstones (Buntsandstein) from the Soultz-sous-Forêts geothermal site (France). *Geotherm. Energy* **2017,** *5*, 26.
(47) Heap, M. J.; Villeneuve, M.; Kushnir, A. R.; Farquharson, J. I.; Baud, P.; Reuschlé, T. Rock mass strength and elastic modulus of the Buntsandstein: an important lithostratigraphic unit for geothermal exploitation in the Upper Rhine Graben. *Geothermics* **2019,** *77*, 236-256.

For Table of Contents Use Only

Manuscript Title

Barite growth rates as a function of crystallographic orientation, temperature, and solution saturation state

Author list

Mélanie Vital, Damien Daval, Gilles Morvan, Daniel E. Martinez, Michael J. Heap

TOC Graphic

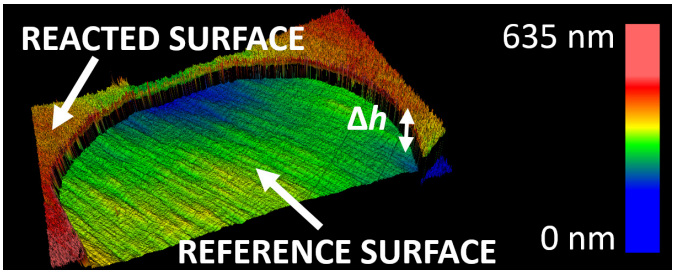

Synopsis

Barite growth rate was monitored as function of crystallographic orientation, temperature, and solution saturation state by measuring the thickness of the grown layer using vertical scanning interferometry